applied sciences

MDPI

Article

Evaluation of 3D Lithospheric Velocity Models Beneath Southern Tianshan–Tarim, China

Qi Cen [1,2] and Han Li [1,2,*]

[1] College of Oceanography, Hohai University, Nanjing 210098, China; cenqi@hhu.edu.cn
[2] Hubei Subsurface Multi-Scale Imaging Key Laboratory, School of Geophysics and Geomatics, China University of Geosciences, Wuhan 430074, China
* Correspondence: lihan2022@hhu.edu.cn

Abstract

The southern Tianshan–Tarim region marks the transition between an active orogenic belt and a relatively stable craton and is therefore important for understanding intracontinental deformation and craton–orogen interactions. We quantitatively evaluate four representative three-dimensional (3D) lithospheric velocity models—XJVM, GNVS, USTC, and CSRM—using three-component broadband records from 34 Mw 5.0–6.0 earthquakes between 2011 and 2022. Path-specific equivalent one-dimensional (1D) models are constructed from velocity profiles beneath each source and station, and synthetic seismograms are calculated using the frequency–wavenumber method. Model performance is assessed using waveform cross-correlation coefficients (CC) and time shifts for radial P (RP), transverse S (TS), and vertical P (ZP) waves in the 0.05–0.2 and 0.05–0.3 Hz bands. Mean CC values decrease from 58.3–64.3% to 53.5–61.5% as the upper frequency increases, indicating larger waveform discrepancies at higher frequencies. XJVM and USTC yield relatively high mean RP correlations, XJVM has the highest mean TS correlations, and GNVS has the highest mean and median ZP correlations in both bands. Absolute mean time shifts remain below 1 s for all models. Overall, model performance varies with frequency band and component, with no single model consistently outperforming the others across all evaluation metrics. These results provide a quantitative basis for model selection, application, and refinement in the southern Tianshan–Tarim region.

Keywords: southern Tianshan–Tarim; three-dimensional lithospheric velocity model; waveform simulation; model evaluation

1. Introduction

Seismic velocity models provide a quantitative representation of the subsurface and constitute an important component of geophysical Earth observation. They help constrain lithospheric composition and architecture, inform interpretations of geodynamic processes, and support earthquake location, source inversion, and seismic wave propagation modeling [1–5]. Growing seismic datasets and improved imaging techniques have yielded multiple three-dimensional (3D) velocity models for many regions [6]. These models differ in their input observations, inversion strategies, parameterization, and imposed constraints, resulting in variations in spatial resolution, anomaly amplitudes, and structural geometry. Comparisons of model structures alone are insufficient to assess how accurately the models predict seismic observations. Evaluating model predictions against independent seismic data using consistent processing and criteria is therefore needed to assess model performance and applicability and guide refinement [1,3,7].

Check for updates

Academic Editor: Guoxin Chen

Received: 21 September 2026
Revised: 15 October 2026
Accepted: 20 October 2026
Published: 23 October 2026

Copyright: © 2026 by the authors. Licensee MDPI, Basel, Switzerland. This article is an open access article distributed under the terms and conditions of the Creative Commons Attribution (CC BY) license.

The southern Tianshan–Tarim transition zone (Figure 1) lies at the junction of the Central Asian Orogenic Belt and the Tarim Craton, marking the boundary between an active orogen and a relatively stable cratonic domain [8,9]. The Tianshan underwent multiple episodes of subduction, accretion, and continental collision during the Paleozoic, followed by renewed uplift and intracontinental deformation in the Cenozoic under far-field stresses associated with the India–Eurasia collision. It continues to accommodate substantial, approximately north–south crustal shortening [10–12]. In contrast, the adjacent Tarim Craton has remained relatively stable during Cenozoic intracontinental convergence [8], although seismic imaging reveals lateral variations in upper-crustal S-wave velocities and subsurface interface geometry within the basin [13]. These contrasts in tectonic architecture and rheology contribute to complex basin–orogen interactions and pronounced lateral heterogeneity in lithospheric structure, making the region a valuable setting for investigating intracontinental mountain building, craton–orogen interactions, and lithospheric dynamics.

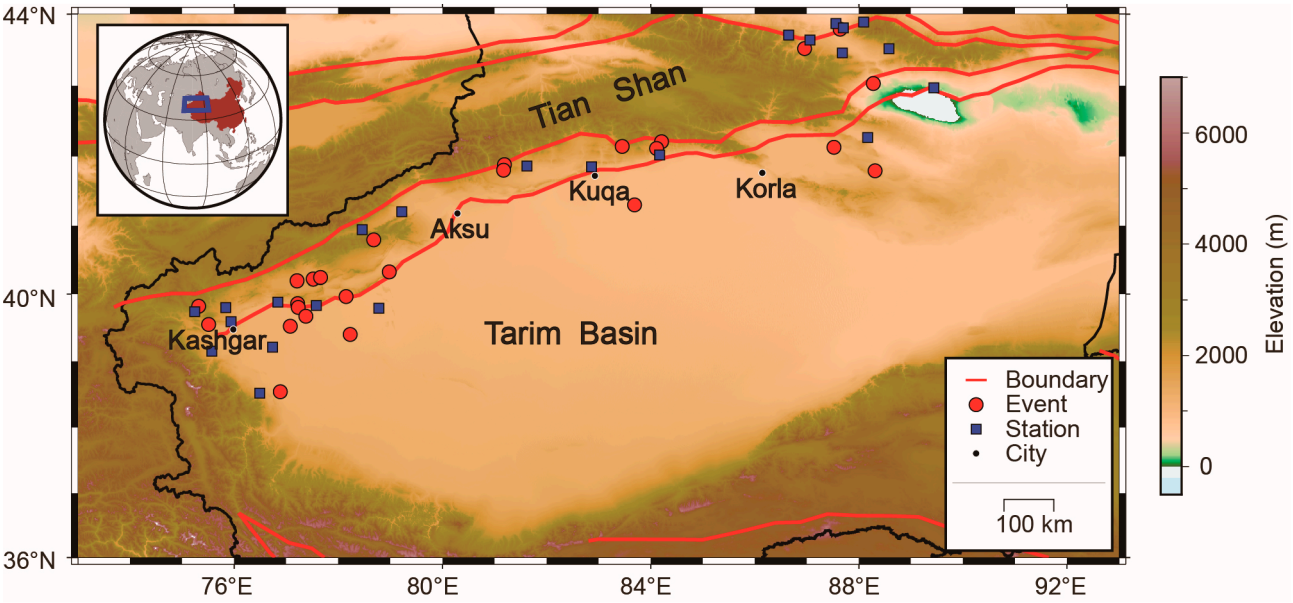


Figure 1. Location, tectonic setting, seismic stations, and earthquake distribution in the southern Tianshan–Tarim region. The blue rectangle in the upper-left inset shows the location of the study area. Red circles denote earthquakes with moment magnitudes (Mw) of 5.0–6.0 occurring between 2011 and 2022 [14,15], blue squares indicate permanent seismic stations used in this study [16], and red lines represent tectonic boundaries [17].

Active-source seismic surveys [18], earthquake tomography [19,20], receiver function analysis [21,22], and surface-wave imaging using earthquake and ambient-noise records [23–26] have provided extensive information on the crust and upper mantle beneath the Tianshan–Tarim region. These studies reveal a complex distribution of high- and low-velocity anomalies [27], although their locations, amplitudes, geometries, and geodynamic interpretations vary among studies [19]. Such differences may reflect variations in station and earthquake distributions, data types, inversion strategies, and spatial resolution. Recent 3D models covering the southern Tianshan–Tarim region include the Xinjiang regional velocity model XJVM-1.0 (hereafter XJVM) [28], the Tianshan shear-wave velocity model Green-Vs (GNVS) [29], the Unified Seismic Tomography Models for Continental China Lithosphere USTClitho2.0 (USTC) [6], and the China Seismological Reference Model CSRM-1.0 (CSRM) [2]. Specifically, XJVM and GNVS focus on Xinjiang and the Tianshan region, respectively, whereas USTC and CSRM provide continental-scale coverage. XJVM and USTC jointly invert body-wave arrival times and surface-wave dispersion, GNVS

derives S-wave velocities from ambient-noise surface-wave observations, and CSRM integrates multiple complementary seismic datasets. Together, they provide a foundation for investigating regional lithospheric structure while raising the question of how consistently they predict observed seismic waveforms.

Comparisons of velocity models commonly use horizontal slices, vertical cross-sections, and the spatial distribution of major anomalies to identify shared features and discrepancies [28]. These comparisons characterize differences in absolute velocities and structural geometry, but agreement among models does not establish their accuracy. Residuals between observed and predicted body-wave travel times provide an observational test [6,28,30], although phase-picking errors and uncertainties in earthquake locations and origin times can influence the results. Surface-wave dispersion measurements offer complementary constraints, with sensitivity to structure that depends on wave type, mode, and period [29]. Comparing observed and synthetic seismograms incorporates information on both timing and waveform shape, allowing model predictions to be assessed within a common computational framework. Previous applications have demonstrated the value of waveform-based evaluation for identifying model strengths and limitations and guiding further refinement [1,7,31].

Despite the availability of several 3D velocity models for the southern Tianshan–Tarim region [2,6,28,29,32], most studies have emphasized model construction and tectonic interpretation. Comparative assessments using the same observations, source parameters, forward-modeling procedure, and evaluation metrics remain limited [1,33,34]. In particular, the extent to which model performance varies with waveform component and frequency band has yet to be systematically assessed. In this study, we evaluate XJVM, GNVS, USTC, and CSRM using three-component broadband recordings of Mw 5.0–6.0 earthquakes that occurred between 2011 and 2022. The principal objectives are:

(1) To quantitatively compare the waveform predictions of the four models using the same observations, source parameters, and equivalent 1D frequency–wavenumber forward-modeling procedure.
(2) To assess how model performance varies between the 0.05–0.2 Hz and 0.05–0.3 Hz bands and among the RP, TS, and ZP components, using waveform cross-correlation coefficients and time shifts.
(3) To identify the relative strengths and limitations of the models for the sampled paths and provide a basis for their selection and application within the constraints of the adopted modeling approach.

2. Representative 3D Velocity Models

We compare four 3D models covering the study area: the regional XJVM and GNVS models and the continental-scale USTC and CSRM models. Table 1 summarizes their coverage and principal characteristics. Their observational constraints and structural differences are outlined below.

XJVM provides crustal and uppermost-mantle P- and S-wave velocities beneath Xinjiang and adjacent regions [28]. Its joint inversion combines double-difference body-wave tomography and direct surface-wave dispersion inversion with topographic corrections [35]. The ak135 reference model [36] was used for theoretical travel time calculations. Rayleigh-wave group and phase dispersion span 5–50 s. Checkerboard tests indicate lateral resolution of approximately 50 km beneath the Tianshan and basin margins and 100 km within the basins; vertical resolution coarsens from approximately 10 to 20 km with depth. These resolution differences constrain the scale of geological interpretation: smaller-scale structures are less well resolved within the basins and at greater depths. Consequently, smoother velocity patterns in these regions should not be interpreted as evidence of greater geological

homogeneity. Its regional focus and joint P- and S-wave constraints are useful for investigating Xinjiang, although its coarser resolution within the basins and at greater depths limits the detail that can be resolved [28].

Table 1. Details of the four representative 3D velocity models in the study area.

Model Name	Data and Method Used in Deriving Model	Horizontal Spacing	Depth	Region
XJVM [28]	Body-wave travel time + Rayleigh-wave dispersion (5~50 s)	0.5° × 0.5°	0~225 km	Xinjiang
GNVS [29]	Rayleigh-wave dispersion (2~60 s)	0.4° × 0.4°	2~70 km	Xinjiang
USTC [6]	Body-wave travel time + Rayleigh-wave dispersion (8~70 s)	0.5° × 0.5°	0~150 km	China
CSRM [2]	P-wave polarization + Rayleigh-wave ellipticity and dispersion (8–70 s) + Receiver function + Ambient-noise Green's function + Pn travel time	0.4° × 0.4°	0~120 km	China

GNVS provides S-wave velocities beneath the Tianshan and surrounding regions [29]. It uses two years of continuous recordings from 224 stations. Ambient-noise cross-correlation following Bensen et al. [37] and selective stacking yielded 24,851 empirical Green's functions. The model has a horizontal spacing of approximately 0.4°. GNVS provides regional constraints on S-wave structure from ambient-noise observations, but its limited spatial coverage and lack of independently determined P-wave velocities restrict its application to P-wave modeling [29].

USTC represents crustal and upper-mantle velocities beneath continental China [6]. It updates the double-difference tomography model USTClitho1.0 of Xin et al. [30] through joint inversion of P- and S-wave first-arrival times and Rayleigh-wave dispersion at periods of 8–70 s. Its reported lateral resolution is approximately 0.5–1.0°, with improved imaging in regions of pronounced topography. Its continental-scale coverage and joint body- and surface-wave inversion provide a consistent framework for regional comparisons, although its resolution limits the representation of small-scale structures [6].

CSRM is a crustal and upper-mantle reference model for China developed by Xiao et al. [2]. It integrates teleseismic P-wave polarization, Rayleigh-wave ellipticity and dispersion, receiver functions, ambient-noise Green's functions, and Pn travel times using observations from 4435 stations. Reported resolution is approximately 60–120 km in the crust and 300 km in the upper mantle. Its diverse observations provide complementary constraints on crustal and upper-mantle structure, although its substantially coarser upper-mantle resolution limits detailed interpretation at greater depths [2].

All three P-wave velocity models exhibit pronounced lateral heterogeneity within the study area (Figure 2). At depths of 10–20 km, XJVM and USTC show broadly similar spatial patterns across the investigated depths, with closer spatial correspondence at 10–20 km. Nevertheless, the extent of the relatively low-velocity regions and the absolute velocity values within their central parts differ between the two models. CSRM also shows relatively low velocities beneath the central basin at shallow depths but features pronounced high-velocity anomalies in the west and northwest. At depths of 30–40 km, the central parts of XJVM and USTC transition from relatively low to relatively high velocities, whereas CSRM exhibits stronger lateral variations, particularly prominent high-velocity anomalies in the central and eastern parts of the study area. Model differences become more pronounced at 60 km depth: CSRM displays a relatively continuous high-velocity structure in the central and eastern regions, while XJVM and USTC show smoother velocity variations or more localized anomalies. Overall, the models share some shallow features but differ more

substantially in anomaly geometry and amplitude at depths of 30–60 km. These inter-model differences alone do not establish the degree of compositional or structural heterogeneity in the crust. Along a central Tien Shan–Tarim profile, Zhang et al. [21] imaged the Moho at approximately 50 km beneath the Tarim sector and 65–70 km beneath the South-Central Tien Shan. Thus, the 60-km slices may sample upper-mantle or lower-crustal material, depending on location. Composition also affects velocity: under comparable pressure and temperature conditions, mafic crustal rocks generally have higher P-wave velocities than felsic rocks [38]. However, velocity alone does not uniquely determine lithology; data constraints, resolution, and the representation of crustal interfaces also contribute to inter-model differences.

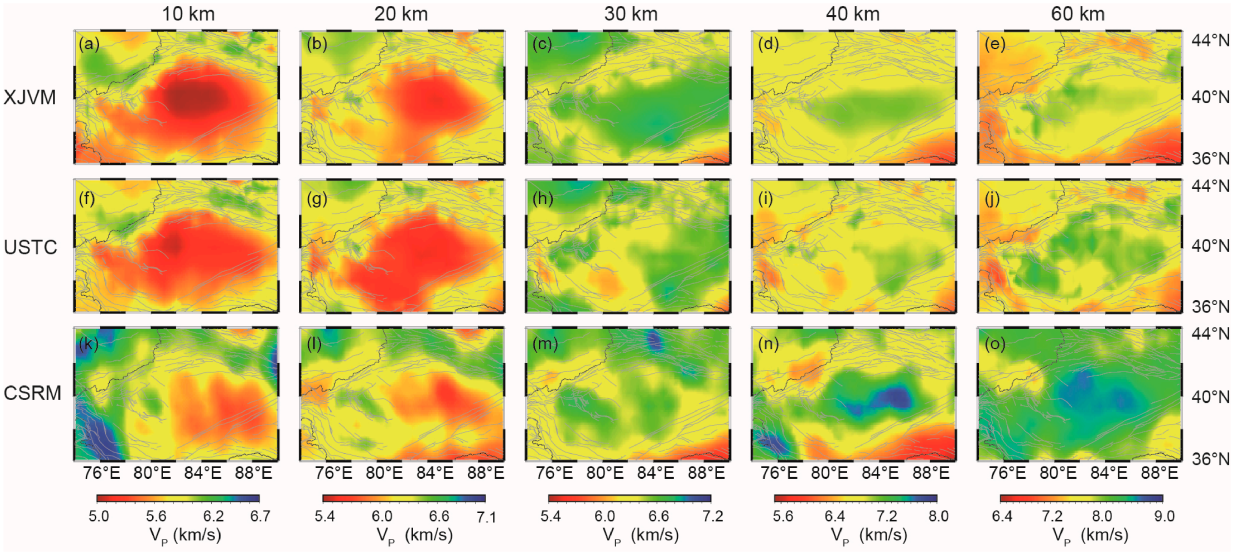


Figure 2. P-wave velocity (V_P) distributions at depths of 10, 20, 30, 40, and 60 km for the (**a**–**e**) XJVM, (**f**–**j**) USTC, and (**k**–**o**) CSRM models.

Figure 3 presents absolute S-wave velocities at depths of 10, 20, 30, 40, and 60 km within the southern Tianshan–Tarim region. The models share some broad spatial features but differ in the locations, lateral extents, and absolute velocities of relatively high- and low-velocity regions at individual depths. These differences reflect both the structures represented by each model and differences in observational constraints and inversion procedures. At 10–20 km depth, XJVM and USTC show similar patterns, with relatively low velocities beneath the central and northern Tarim Basin and higher velocities in the surrounding regions. CSRM displays smoother shallow velocity variations but likewise indicates relatively low velocities within the basin. At depths of 30–40 km, the low-velocity anomalies beneath the basin become less pronounced, while relatively high-velocity structures emerge in the central and eastern parts of XJVM and USTC. In CSRM, high-velocity anomalies in these areas are particularly prominent at 40 km depth. At 60 km depth, differences among the models become more pronounced in the locations, spatial extents, and amplitudes of the anomalies. Although GNVS has limited spatial coverage, it also exhibits substantial lateral velocity variations within its coverage area.

Geologically, the relatively low velocities beneath the basin at shallower depths may partly reflect sedimentary cover, whereas higher velocities at greater depths may be associated with crystalline basement and, where the Moho is shallower than the sampling depth, upper-mantle material. Zhang et al. [28] interpreted the broad velocity contrasts between the Tarim Basin and the Tianshan in terms of differences between the relatively rigid cratonic domain and the deformed orogenic crust. These interpretations provide a possible geological context for the shared large-scale patterns. However, discrepancies

among models should not be assigned separate geological origins without independent constraints, because resolution, parameterization, and the representation of crustal interfaces can also affect the imaged velocity patterns.

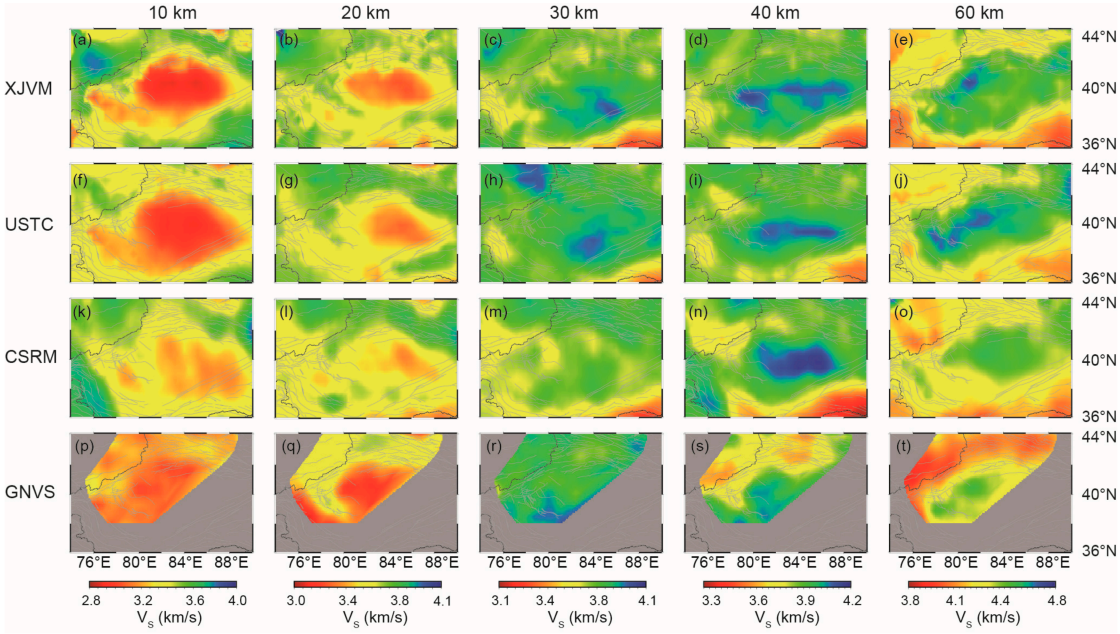


Figure 3. S-wave velocity (V_S) distributions at depths of 10, 20, 30, 40, and 60 km for the (**a**–**e**) XJVM, (**f**–**j**) USTC, (**k**–**o**) CSRM, and (**p**–**t**) GNVS models. Gray areas indicate regions outside the GNVS model coverage.

3. Data and Methods

3.1. Seismic Data and Forward Modeling of Synthetic Seismograms

Three-component broadband waveform records for 34 Mw 5.0–6.0 earthquakes that occurred in the southern Tianshan–Tarim region between 2011 and 2022 were obtained from the National Earthquake Data Center [16]. To ensure comparability across velocity models, the same source parameters were used to calculate synthetic seismograms for each event. Earthquake locations, source depths, moment tensors, and parameters describing the source time functions were taken from the Global Centroid Moment Tensor (GCMT) catalog [15]. Figure 1 shows the spatial distribution of the earthquakes and seismic stations.

Synthetic seismograms for a point source in a horizontally layered medium were calculated using the frequency–wavenumber (F–K) method [39]. This method uses propagator matrices to solve the elastic wave response of a multilayered medium, allowing complete synthetic waveforms to be computed at different distances and for different components. Because the F–K method assumes horizontal layering, 3D velocity models cannot be used directly as inputs. To assess waveform predictions for the selected event–station paths, we restricted the analysis to pairs with epicentral distances of less than 100 km and constructed a path-specific equivalent 1D structure from each of the XJVM, GNVS, USTC, and CSRM models.

The four 3D models were interpolated onto a common horizontal grid and common depth nodes. At each depth node, P- and S-wave velocities were extracted beneath the source and station locations, and their arithmetic means were calculated as $\overline{V}(\mathcal{Z}_i) = \frac{V^{src}(\mathcal{Z}_i)+V^{sta}(\mathcal{Z}_i)}{2}$, where V^{src} and V^{sta} denote the velocity structures beneath the source and station, respectively, and $\overline{V}$ denotes the equivalent 1D structure for the corresponding event–station pair. All other forward-modeling parameters were kept identical across models so that differences in the synthetic seismograms primarily reflected differ-

ences in velocity structure. For GNVS, which provides only S-wave velocities, P-wave velocities were estimated as $V_P/V_S = \sqrt{3}$, assuming a Poisson solid with a Poisson's ratio of 0.25 [40]. Three-component synthetic seismograms were then calculated for each event–station pair using the equivalent 1D structures derived from XJVM, GNVS, USTC, and CSRM.

3.2. Quantitative Model Evaluation

To quantitatively assess the reliability of the velocity models, we use waveform cross-correlation coefficients (CC) and time shifts (τ) between synthetic and observed seismograms. The waveform cross-correlation coefficient is defined as follows [1]:

$$CC = \frac{\int_{t_1}^{t_2} [\mathrm{obs}(t) \cdot \mathrm{syn}(t-\tau)]\mathrm{d}t}{\sqrt{\int_{t_1}^{t_2} \mathrm{obs}^2(t)\mathrm{d}t \cdot \int_{t_1}^{t_2} \mathrm{syn}^2(t)\mathrm{d}t}} \times 100\%, \quad (1)$$

where obs(t) and syn(t) denote the observed and synthetic seismograms, respectively, and t_1 and t_2 define the time window used to calculate CC. A higher CC indicates greater waveform similarity and, under the adopted modeling conditions, better predictive performance of the corresponding velocity model. The time shift (τ) is defined as the observed arrival time minus the predicted arrival time [41], i.e., $\tau = t(\mathrm{obs}) - t(\mathrm{syn})$. A negative ($\tau$) indicates that the observed phase arrives earlier than the synthetic phase, corresponding to an overestimated travel time; a positive τ indicates that the observed phase arrives later. For each model, frequency band, and waveform component, we calculated the mean, standard deviation, median, and median absolute deviation of CC and (τ). We also counted the samples satisfying CC > 60% and $|\tau| < 6$ s, respectively, to compare how well the model predictions reproduce the observed records.

For each earthquake, we selected station records with epicentral distances of less than 100 km and relatively high signal-to-noise ratios. After checks for data quality and completeness, the raw waveforms were demeaned, detrended, corrected for instrument response, and rotated into radial, transverse, and vertical components. Following Wang et al. [1], we compared observed and synthetic waveforms in two frequency bands: 0.05–0.2 Hz and 0.05–0.3 Hz. The 0.05–0.2 Hz band was used primarily to assess the models' ability to reproduce longer-period waveforms associated with broad crustal velocity structure. Here, regional-scale structure refers to large-scale velocity variations across the southern Tianshan–Tarim region, including the overall contrasts between the basin and the adjacent orogenic belt, rather than individual faults or small-scale heterogeneities. Extending the upper frequency limit to 0.3 Hz incorporates higher-frequency waveform content with greater sensitivity to shallow structures and smaller-scale velocity variations. Identical filtering, windowing, and peak-amplitude normalization procedures were applied to the observed and synthetic seismograms to minimize the influence of processing differences on model comparisons. The analysis focused on windows around the initial P-wave arrivals on the radial (RP) and vertical (ZP) components, and the initial S-wave arrivals on the transverse component (TS). These arrivals are relatively easy to identify in the observed records and are less prone to interference from other phases. The 1D velocity profile extracted from CRUST1.0 [42] was also used as a reference for forward modeling and waveform comparison, providing a baseline for evaluating the four 3D velocity models.

4. Results

4.1. Waveform Cross-Correlation Coefficients

For the 30 August 2013 Mw 5.3 earthquake recorded at XJ.WMQ (with epicentral distance of 5.32 km and azimuth of 65.27°), all four 3D models reproduced the principal

waveform features (Figures 4 and 5). For all 3D models, (1) in the 0.05–0.2 Hz band, CC exceeds 88% for all components and 95% for ZP; (2) extending the band to 0.05–0.3 Hz reduces RP and TS correlations, while ZP correlations remain at or above 93%. This example illustrates the component and frequency dependence examined across the full dataset below.

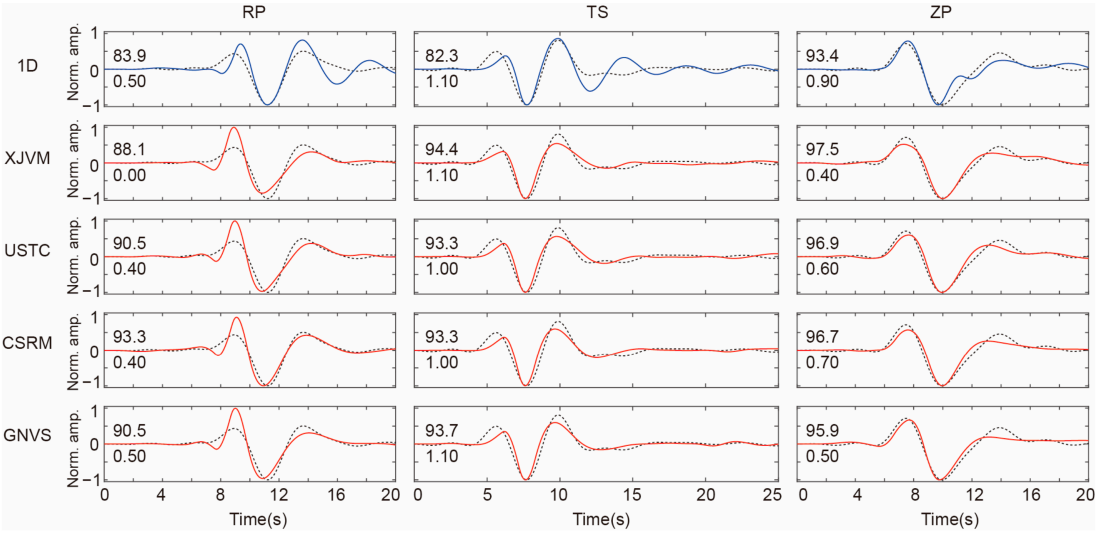


Figure 4. Comparison of normalized observed waveforms (dashed lines) recorded at station XJ.WMQ (with epicentral distance of 5.32 km and azimuth of 65.27°) for the 30 August 2013 Mw 5.3 earthquake and synthetic seismograms (blue solid line: 1D reference model, red solid lines: 3D models) in the 0.05–0.2 Hz frequency band. Rows show results for the 1D reference model, XJVM, USTC, CSRM, and GNVS, from top to bottom. Columns show radial-component P waves (RP), transverse-component S waves (TS), and vertical-component P waves (ZP), from left to right. In each panel, CC values (%) are shown above the waveforms, and time shifts (s) are shown below.

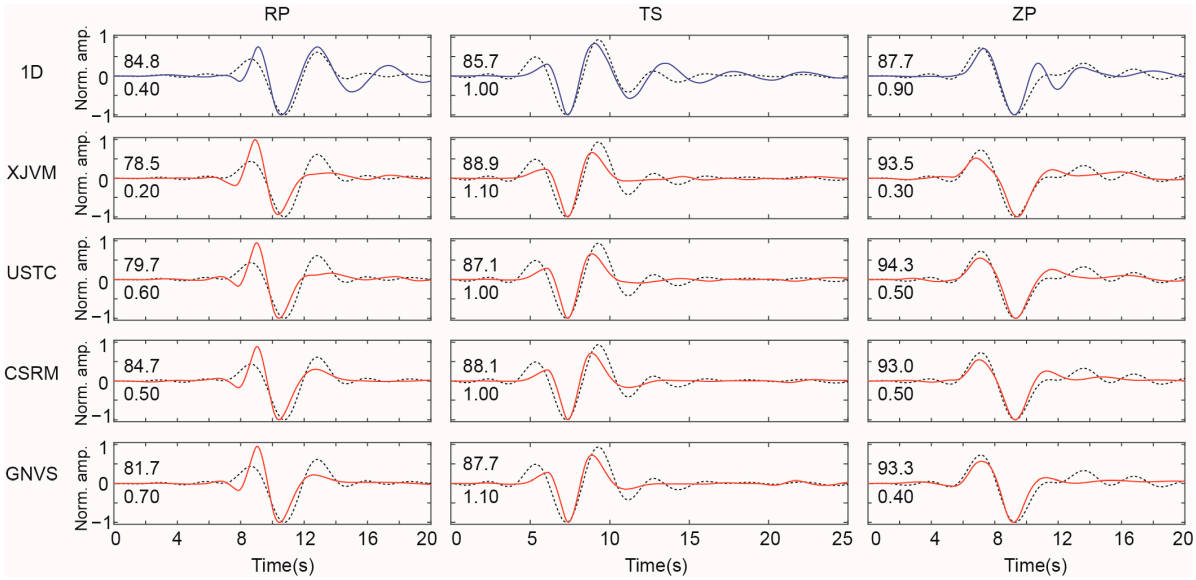


Figure 5. Same as Figure 4, but for the 0.05–0.3 Hz frequency band.

To further compare overall model performance across all event–station pairs, we examined the CC distributions for the RP, TS, and ZP components in both frequency bands (Figures 6 and 7), with the corresponding mean values summarized in Table 2. In the 0.05–0.2 Hz band, mean CC values across all models and components range from 57.7% to 64.3%. When the band is extended to 0.05–0.3 Hz, this range decreases to 53.4–61.5%.

Mean CC decreases for all three components of every model as the upper frequency limit increases.

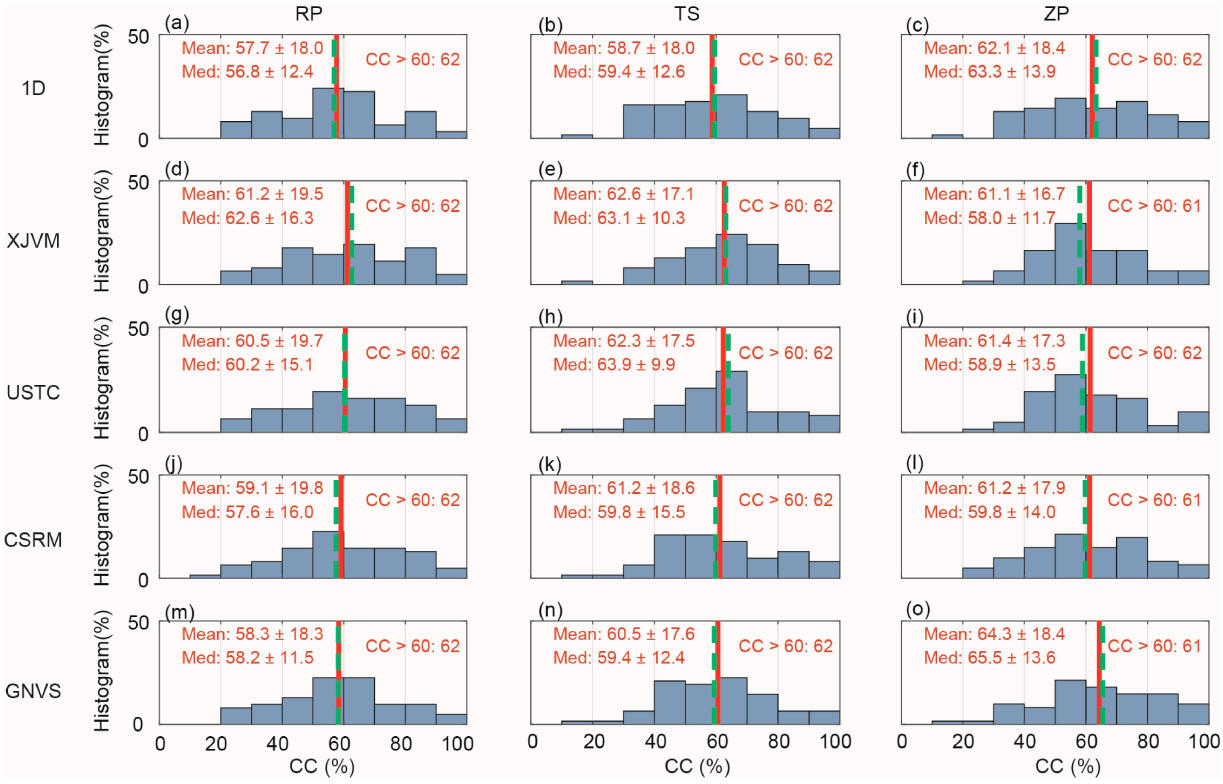


Figure 6. Histograms of waveform CC in the 0.05–0.2 Hz frequency band for (**a**–**c**) the 1D reference model, (**d**–**f**) XJVM, (**g**–**i**) USTC, (**j**–**l**) CSRM, and (**m**–**o**) GNVS. Columns correspond to the RP, TS, and ZP components, from left to right. Histogram heights indicate the percentage of samples in each CC bin. "Mean" and "Med" report the mean ± standard deviation and median ± median absolute deviation, respectively. "CC > 60" denotes the number of samples with CC > 60%. Red solid and green dashed vertical lines indicate the mean and median, respectively.

Table 2. Mean CC (%) for the RP, TS, and ZP components of the five models in two frequency bands.

Component	Frequency Band (Hz)	XJVM	USTC	CSRM	GNVS	1D
RP	0.05–0.2	61.2	60.5	59.1	58.3	57.7
	0.05–0.3	56.9	56.9	55.4	53.5	53.4
TS	0.05–0.2	62.6	62.3	61.2	60.5	58.7
	0.05–0.3	57.6	56.7	56.8	56.7	56.4
ZP	0.05–0.2	61.1	61.4	61.2	64.3	62.1
	0.05–0.3	58.5	57.5	58.6	61.5	59.1

According to the results in Figures 6 and 7 and Table 2, in the 0.05–0.2 Hz band, XJVM and USTC yield relatively high RP and TS correlations. XJVM has the highest means, at 61.2% for RP and 62.6% for TS. For ZP, GNVS has the highest mean (64.3%) and median (65.5%); the other models have similar mean values. In the 0.05–0.3 Hz band, XJVM and USTC tie for the highest mean RP CC (56.9%). Mean TS CC values converge to 56.4–57.6%, with XJVM remaining slightly higher. GNVS retains the highest mean (61.5%) and median (61.8%) ZP CC.

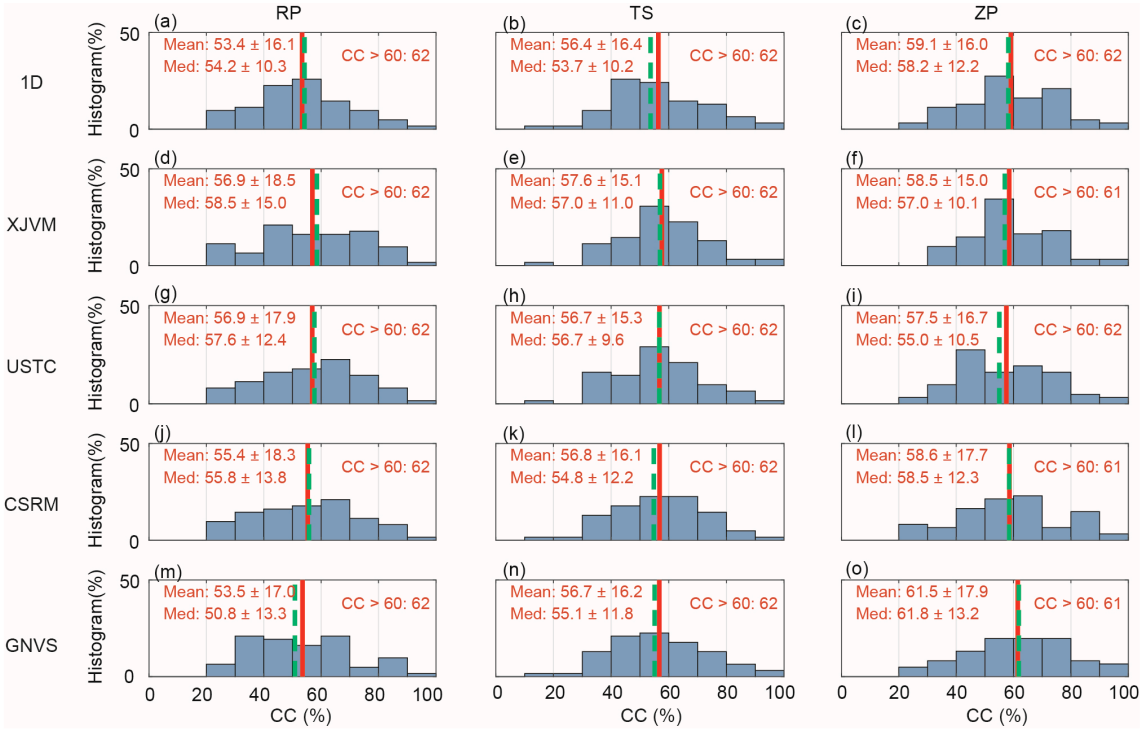


Figure 7. Same as Figure 6, but for the 0.05–0.3 Hz frequency band.

4.2. Time Shifts

Figures 8 and 9 show the time-shift distributions for the different velocity models in the two frequency bands, with mean values summarized in Table 3. Overall, the distributions are centered close to zero, with means ranging from −0.9 to 0.7 s and medians generally between −0.9 and 0.8 s. However, the within-group variability is more pronounced than the small differences in mean values among models, with median absolute deviations mostly ranging from 1.5 to 2.3 s. The numbers of samples satisfying $|\tau| < 6$ s range from 52 to 56 for RP and from 58 to 59 for ZP, compared with 37 to 44 for TS, indicating relatively more samples with large time shifts for the TS component.

Table 3. Mean τ (s) for the RP, TS, and ZP components of the five models in two frequency bands.

Component	Frequency Band (Hz)	XJVM	USTC	CSRM	GNVS	1D
RP	0.05–0.2	−0.5	−0.7	−0.8	−0.2	−0.1
	0.05–0.3	−0.3	−0.4	−0.9	0.4	0.2
TS	0.05–0.2	0.0	0.2	0.1	0.4	−0.1
	0.05–0.3	0.0	0.4	−0.4	0.4	0.4
ZP	0.05–0.2	0.5	0.4	0.6	0.5	0.7
	0.05–0.3	0.3	−0.1	0.4	0.3	0.6

In the 0.05–0.2 Hz band, mean time shifts for RP are negative across all models, ranging from −0.8 to −0.1 s. The 1D model and GNVS are closest to zero, whereas CSRM and USTC show relatively larger negative offsets. For TS, means range from −0.1 to 0.4 s and medians from −0.2 to 0.1 s, indicating similar distribution centers across models. ZP shows a different pattern, with positive mean time shifts of 0.4–0.7 s. Its median absolute deviations range from 1.6 to 1.8 s, smaller than most RP and TS values in the same band. Thus, the distributions in this band generally show negative offsets for RP, near-zero offsets for TS, and positive offsets for ZP.

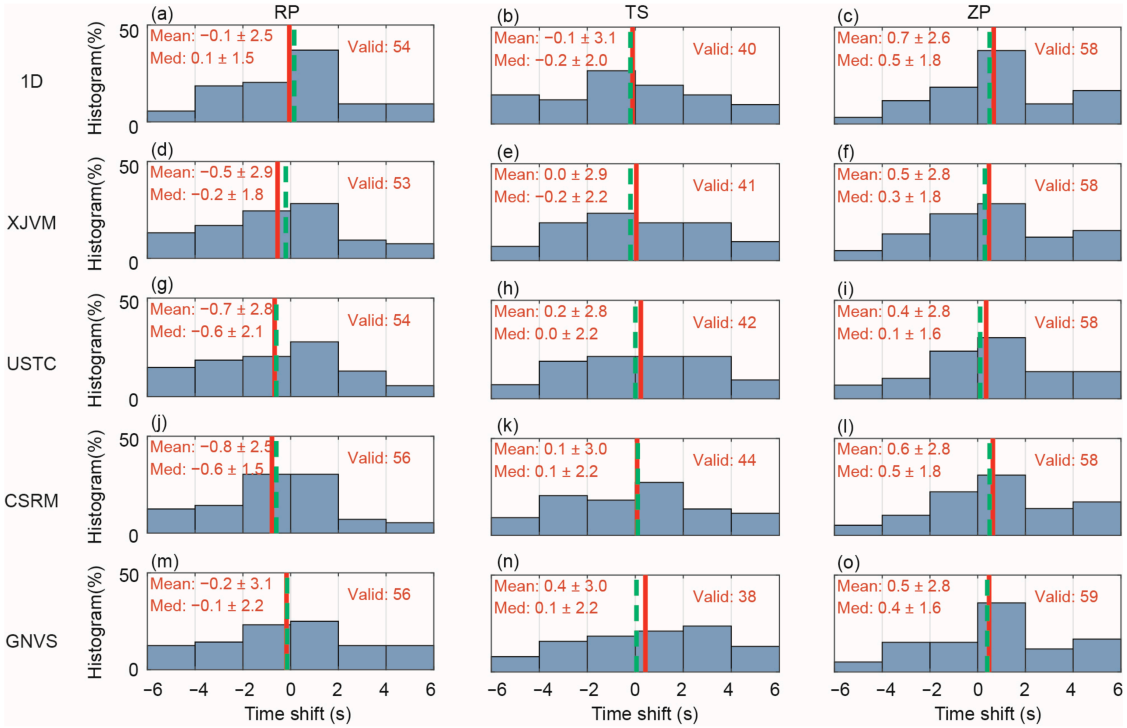


Figure 8. Histograms of time shifts in the 0.05–0.2 Hz frequency band for (**a**–**c**) 1D, (**d**–**f**) XJVM, (**g**–**i**) USTC, (**j**–**l**) CSRM, and (**m**–**o**) GNVS. Columns correspond to the RP, TS, and ZP components, from left to right. Histogram heights indicate the percentage of samples in each time-shift bin. "Mean" and "Med" report the mean ± standard deviation and median ± median absolute deviation, respectively, in seconds. "Valid" denotes the number of samples satisfying $|\tau| < 6$ s. Red solid and green dashed vertical lines indicate the mean and median, respectively.

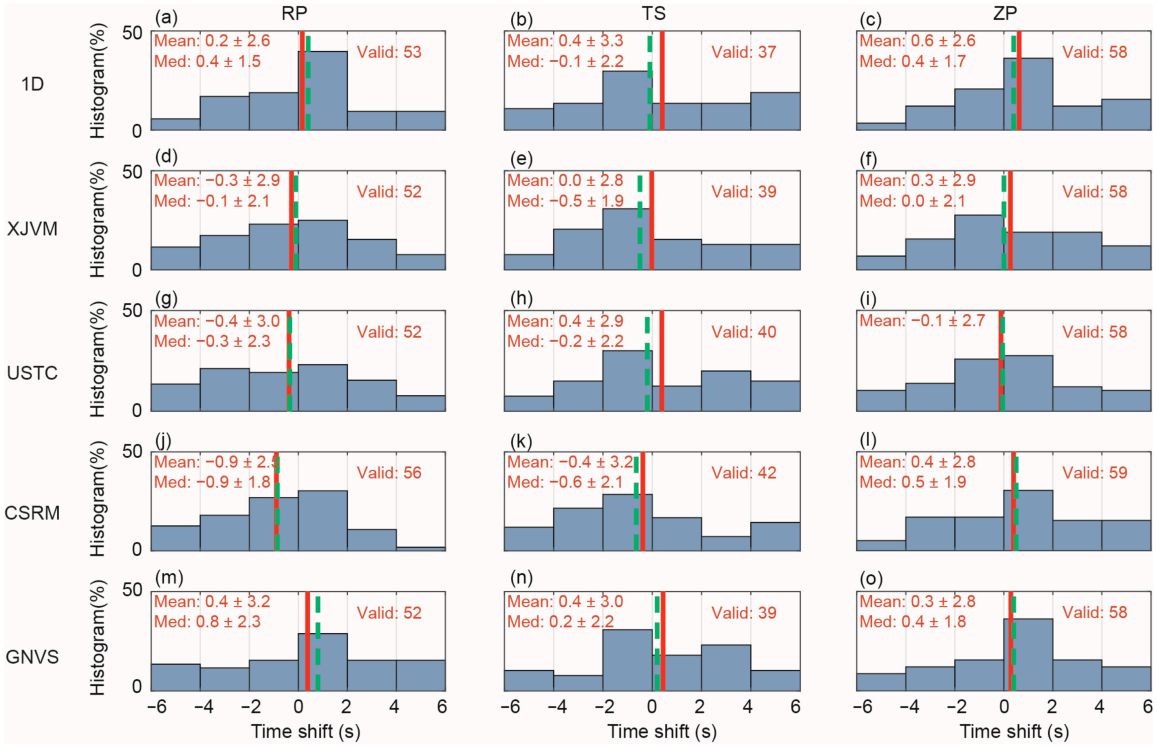


Figure 9. Same as Figure 8, but for the 0.05–0.3 Hz frequency band.

When the band is extended to 0.05–0.3 Hz, mean time shifts remain small, although the relative patterns change. For RP, means range from −0.9 to 0.4 s. XJVM and USTC retain negative values but move closer to zero than in the lower-frequency band. CSRM continues to show a relatively pronounced negative offset, whereas GNVS and the 1D model shift to positive values. For TS, means range from −0.4 to 0.4 s, with XJVM closest to zero, CSRM showing a negative value, and the remaining models showing positive values. ZP retains predominantly small positive mean time shifts, except for USTC, which shows a slight negative value of −0.1 s. Changes in mean time shifts between the two bands do not exceed 0.6 s for any model and show no consistent direction.

No model consistently yields mean shifts closest to zero across bands and components. Because substantial variability remains among individual paths, these means should be interpreted alongside the distributions and waveform correlations.

5. Discussion

The results show that waveform-fitting performance varies with frequency band and component. Extending the frequency band from 0.05–0.2 Hz to 0.05–0.3 Hz reduces mean CC for all models and components, indicating greater discrepancies between observed and synthetic waveforms when higher-frequency content is included. Shorter wavelengths increase sensitivity to smaller-scale heterogeneity and propagation effects that may not be adequately represented by the available models or the adopted modeling approach. Differences in attenuation, scattering, source time functions, and observational noise may also contribute to the lower correlations. Absolute mean time shifts remain below 1 s, indicating small overall signed timing biases, although individual records exhibit substantial variability. Thus, small average timing biases coexist with differences in waveform similarity after time alignment. These results support evaluating model performance for specific frequency bands and waveform components.

(1) RP component: The radial and vertical waveforms within the selected P-wave windows respond differently to source radiation, incidence angle, shallow structure, and free-surface effects, including P–SV conversions. Their correlations therefore provide distinct measures of waveform agreement. The relatively high RP correlations of XJVM and USTC may reflect their combined use of body-wave arrival times and Rayleigh-wave dispersion, which provide complementary structural constraints. XJVM incorporates regionally focused observations [28], although its small advantage in mean CC does not establish a substantial difference in overall accuracy. The pronounced lateral variations in CSRM [2] may be less fully represented by the equivalent 1D profiles, potentially affecting its waveform predictions. For GNVS, P-wave velocities are derived from S-wave velocities using a fixed V_P/V_S ratio of $\sqrt{3}$. This conversion preserves the relative pattern of S-wave velocity variations but excludes spatial variations in V_P/V_S documented in continental-scale studies [43]. Its RP performance therefore reflects both the original S-wave model [29] and the imposed velocity conversion.

(2) TS component: In the isotropic, horizontally layered F–K framework, transverse SH motion is decoupled from P–SV motion and provides a relatively direct test of S-wave predictions. XJVM and USTC combine S-wave arrival times and Rayleigh-wave dispersion, whereas GNVS relies on ambient-noise surface waves. Their differing sensitivities may explain why GNVS does not share its ZP advantage for TS. XJVM has the highest mean TS CC, but the narrow inter-model range in the broader band limits discrimination. Mean shifts remain close to zero, while fewer samples satisfy $|\tau| < 6$ s than for RP and ZP, indicating greater variability in TS timing among paths.

(3) ZP component: GNVS yields the highest mean and median ZP correlations in both frequency bands, indicating favorable waveform agreement under the adopted velocity conversion and modeling conditions. Because its P-wave velocities are derived from S-wave velocities, this result does not independently demonstrate a more accurate P-wave structure. The relatively similar ZP correlations of the other models provide less distinction among their predictions for the sampled paths. The GNVS advantage is consequently best interpreted as improved agreement in the time-aligned ZP waveforms rather than superiority across all evaluation metrics.

A comparison with the previous evaluation by Zhang et al. [28] provides additional context for these findings. Their tests showed better agreement with regional earthquake observations for XJVM than for USTC, including smaller mean and standard deviation of body-wave travel-time residuals in a test using 17 earthquakes not included in the inversion. Our results are broadly consistent with this comparison: XJVM and USTC yield similar RP and TS correlations, with a modest CC advantage for XJVM in several comparisons, while XJVM has mean RP and TS time shifts closer to zero in both frequency bands. However, this advantage is not uniform across components, as USTC yields mean ZP time shifts closer to zero. By combining CC with time shifts, our analysis complements the previous travel-time-based evaluation with information on waveform similarity and its frequency and component dependence. Differences in the datasets and forward-modeling approaches nevertheless limit direct quantitative comparison.

For practical applications, XJVM and USTC are useful initial candidates for modeling RP and TS waveforms along the sampled paths and within the investigated frequency bands. GNVS provides a complementary option for ZP waveform modeling, with its performance interpreted in conjunction with the imposed V_P/V_S conversion. Model selection should therefore be guided by the target waveform components and frequency range. The highest correlation for an individual component does not establish that a model is optimal for all source-inversion applications or throughout the study region.

The applicability of these results is primarily constrained by the forward-modeling approximation, spatial data coverage, and uncertainties in source parameters. To accommodate the assumptions of the F–K method, the 3D velocity models were converted into equivalent 1D structures for each event–station pair. This approach allows consistent comparisons among models but cannot fully preserve lateral velocity variations along the actual propagation paths or account for 3D wave-field effects associated with basin boundaries, undulating velocity interfaces, and small-scale anomalies. In addition, the 34 earthquakes and available stations are unevenly distributed, so the results primarily reflect model performance along the sampled paths. Their regional representativeness requires further assessment using additional observations. Using the same GCMT source parameters across models helps control source-related differences in the comparisons, but uncertainties in source location, depth, and focal mechanism may still affect CC and time shifts. Future work could expand event–station path coverage, conduct source parameter perturbation tests, and incorporate fully 3D waveform simulations to further assess the robustness of the findings and the spatial applicability of the velocity models.

6. Conclusions

Using three-component broadband records from 34 earthquakes, we evaluated four 3D lithospheric velocity models beneath the southern Tianshan–Tarim region through a common equivalent 1D forward-modeling framework. The main findings are as follows:

(1) Waveform agreement depends on frequency band. Mean CC decreases for every model and component when the upper frequency limit increases from 0.2 to 0.3 Hz,

indicating greater discrepancies between observed and synthetic waveforms when higher-frequency content is included.

(2) Relative model performance varies among components. XJVM and USTC yield relatively high RP correlations, with similar mean values. XJVM has the highest mean TS CC in both bands, although inter-model differences decrease in the broader band. GNVS yields the highest mean and median ZP correlations, but this result is conditional on the adopted conversion from S-wave to P-wave velocities and does not independently establish a more accurate P-wave structure.

(3) Absolute mean time shifts remain below 1 s for all models, indicating small overall signed timing biases despite substantial variability among individual records. XJVM has mean RP and TS time shifts closer to zero than USTC in both bands, whereas USTC has mean ZP shifts closer to zero. Thus, no model performs best across all metrics, and timing and waveform similarity should be considered together.

These findings support model selection for the sampled paths, components, and frequency bands under the adopted equivalent 1D approximation. Broader observational coverage and fully 3D waveform simulations are needed to assess their regional applicability.

Author Contributions: Conceptualization, H.L.; methodology, Q.C. and H.L.; software, Q.C. and H.L.; validation, Q.C.; formal analysis, H.L.; investigation, Q.C.; resources, H.L.; data curation, H.L.; writing—original draft preparation, Q.C. and H.L.; writing—review and editing, H.L.; visualization, Q.C.; supervision, H.L.; funding acquisition, H.L. All authors have read and agreed to the published version of the manuscript.

Funding: This work was funded by the Deep Earth Probe and Mineral Resources Exploration—National Science and Technology Major Project, grant number 2024ZD1003401, and the Hubei Subsurface Multi-Scale Imaging Key Laboratory, grant number SMIL-2024-02.

Data Availability Statement: All seismic raw data used in this study were obtained from the National Earthquake Data Center (http://data.earthquake.cn). The XJVM and CSRM models are available from Zenodo (https://doi.org/10.5281/zenodo.17287992 (accessed on 15 October 2026); https://doi.org/10.5281/zenodo.8103561 (accessed on 15 October 2026). The USTC model is available from https://github.com/ShouchengHan/USTClitho2.0 (accessed on 15 October 2026), and the GNVS model is archived at https://data.earthquake.cn/datashare/report.shtml?PAGEID=datasourcelist&dt=ff808082989d422c0198df31d1b80003 (accessed on 15 October 2026). The CRUST1.0 model is available at https://igppweb.ucsd.edu/~gabi/crust1.html (accessed on 15 October 2026).

Acknowledgments: The authors are grateful to the editor and anonymous reviewers for their constructive comments that greatly improved this study. Generic Mapping Tools (GMT version 6.5.0) software [44] was used for drawing the graphics in this study. We thank the China Earthquake Networks Center for providing earthquake waveform data.

Conflicts of Interest: The authors declare no conflicts of interest.

Abbreviations

The following abbreviations are used in this manuscript:

XJVM —Xinjiang regional velocity model (XJVM-1.0) [28]
USTC —Unified Seismic Tomography Models for Continental China Lithosphere (USTClitho2.0) [6]
CSRM —China Seismological Reference Model (CSRM-1.0) [2]
GNVS —Tianshan shear-wave velocity model (Green-Vs) [29]

References

1. Wang, X.; Chen, L.; Chen, Q. Evaluation of 3D Crustal Seismic Velocity Models in Southwest China: Model Performance, Limitation, and Prospects. *Sci. China Earth Sci.* **2024**, *67*, 604–619. [CrossRef]
2. Xiao, X.; Cheng, S.; Wu, J.; Wang, W.; Sun, L.; Wang, X.; Ma, J.; Tong, Y.; Liang, X.; Tian, X.; et al. CSRM-1.0: A China Seismological Reference Model. *J. Geophys. Res. Solid Earth* **2024**, *129*, e2024JB029520. [CrossRef]
3. Jiang, X.; Song, X.; Li, J.; Zhang, X. Evaluating Lithospheric Velocity Models in the Sichuan–Yunnan Region of China with Full-Waveform Simulations. *Seismol. Res. Lett.* **2026**, *97*, 2520–2536. [CrossRef]
4. Li, H.; Chang, X. A Review of the Microseismic Focal Mechanism Research. *Sci. China Earth Sci.* **2021**, *64*, 351–363. [CrossRef]
5. Li, H.; Yao, Z. Microseismic Focal Mechanism Inversion in Frequency Domain Based on General Dislocation Point Model. *Chin. J. Geophys.* **2018**, *61*, 905–916. [CrossRef]
6. Han, S.; Zhang, H.; Xin, H.; Shen, W.; Yao, H. USTClitho2.0: Updated Unified Seismic Tomography Models for Continental China Lithosphere from Joint Inversion of Body-Wave Arrival Times and Surface-Wave Dispersion Data. *Seismol. Res. Lett.* **2022**, *93*, 201–215. [CrossRef]
7. Lu, Y.; Ben-Zion, Y. Validation of Seismic Velocity Models in Southern California with Full-Waveform Simulations. *Geophys. J. Int.* **2022**, *229*, 1232–1254. [CrossRef]
8. Yang, W.; Xu, Y.; Zhang, L.; Yu, C.; Yu, P.; Zhang, B.; Yang, B. Magnetotellruic Investigation and 3D Lithospheric Structures in the Tarim Terrane. *Acta Geol. Sin.* **2015**, *89*, 1151–1161.
9. Kosarev, G.L.; Petersen, N.V.; Vinnik, L.P.; Roecker, S.W. Receiver Functions for the Tien Shan Analog Broadband Network: Contrasts in the Evolution of Structures across the Talasso-Fergana Fault. *J. Geophys. Res. Solid Earth* **1993**, *98*, 4437–4448. [CrossRef]
10. Kaban, M.K.; Yuanda, T.R. Density Structure, Isostatic Balance and Tectonic Models of the Central Tien Shan. *Surv. Geophys.* **2014**, *35*, 1375–1391. [CrossRef]
11. Pan, Y.; Jiang, W.; Ding, H.; Shum, C.K.; Jiao, J.; Li, J. Intradecadal Fluctuations and Three-Dimensional Crustal Kinematic Deformation of the Tianshan and Pamir Derived From Multi-Geodetic Imaging. *J. Geophys. Res. Solid Earth* **2023**, *128*, e2022JB025325. [CrossRef]
12. Avouac, J.P.; Tapponnier, P.; Bai, M.; You, H.; Wang, G. Active Thrusting and Folding along the Northern Tien Shan and Late Cenozoic Rotation of the Tarim Relative to Dzungaria and Kazakhstan. *J. Geophys. Res.* **1993**, *98*, 6755–6804. [CrossRef]
13. Li, W.; Wang, X.; Liang, X.; Zuo, S.; Li, S.; Qu, C.; Tian, X.; Chen, L. Heterogeneous Tarim Cratonic Crust Induced by a Mantle Plume and Its Effect on Later Tectonic Evolution Based on Multi-Frequency Receiver Functions Imaging. *J. Geophys. Res. Solid Earth* **2024**, *129*, e2024JB029579. [CrossRef]
14. Dziewonski, A.M.; Chou, T.-A.; Woodhouse, J.H. Determination of Earthquake Source Parameters from Waveform Data for Studies of Global and Regional Seismicity. *J. Geophys. Res. Solid Earth* **1981**, *86*, 2825–2852. [CrossRef]
15. Ekström, G.; Nettles, M.; Dziewoński, A.M. The Global CMT Project 2004–2010: Centroid-Moment Tensors for 13,017 Earthquakes. *Phys. Earth Planet. Inter.* **2012**, *200–201*, 1–9. [CrossRef]
16. Data Sharing Infrastructure of National Earthquake Data Center. Available online: http://data.earthquake.cn (accessed on 15 October 2026).
17. Zhang, P.; Deng, Q.; Zhang, G.; Ma, J.; Gan, W.; Min, W.; Mao, F.; Wang, Q. Active Tectonic Blocks and Strong Earthquakes in the Continent of China. *Sci. China Ser. D Earth Sci.* **2003**, *46*, 13–24. [CrossRef]
18. Gao, R.; Hou, H.; Cai, X.; Knapp, J.H.; He, R.; Liu, J.; Xiong, X.; Guan, Y.; Li, W.; Zeng, L.; et al. Fine Crustal Structure beneath the Junction of the Southwest Tian Shan and Tarim Basin, NW China. *Lithosphere* **2013**, *5*, 382–392. [CrossRef]
19. Lei, J. Seismic Tomographic Imaging of the Crust and Upper Mantle under the Central and Western Tien Shan Orogenic Belt. *J. Geophys. Res. Solid Earth* **2011**, *116*, B09305. [CrossRef]
20. Xu, Y.; Liu, F.; Liu, J.; Chen, H. Crust and Upper Mantle Structure beneath Western China from P Wave Travel Time Tomography. *J. Geophys. Res. Solid Earth* **2002**, *107*, ESE 4-1–ESE 4-15. [CrossRef]
21. Zhang, B.; Bao, X.; Xu, Y. Distinct Orogenic Processes in the South- and North-Central Tien Shan From Receiver Functions. *Geophys. Res. Lett.* **2020**, *47*, e2019GL086941. [CrossRef]
22. Vinnik, L.P.; Reigber, C.; Aleshin, I.M.; Kosarev, G.L.; Kaban, M.K.; Oreshin, S.I.; Roecker, S.W. Receiver Function Tomography of the Central Tien Shan. *Earth Planet. Sci. Lett.* **2004**, *225*, 131–146. [CrossRef]
23. Gilligan, A.; Roecker, S.W.; Priestley, K.F.; Nunn, C. Shear Velocity Model for the Kyrgyz Tien Shan from Joint Inversion of Receiver Function and Surface Wave Data. *Geophys. J. Int.* **2014**, *199*, 480–498. [CrossRef]
24. Lü, Z.; Gao, H.; Lei, J.; Yang, X.; Rathnayaka, S.; Li, C. Crustal and Upper Mantle Structure of the Tien Shan Orogenic Belt from Full-Wave Ambient Noise Tomography. *J. Geophys. Res. Solid Earth* **2019**, *124*, 3987–4000. [CrossRef]
25. Zheng, X.; Jiao, W.; Zhang, C.; Wang, L. Short-Period Rayleigh-Wave Group Velocity Tomography through Ambient Noise Cross-Correlation in Xinjiang, Northwest China. *Bull. Seismol. Soc. Am.* **2010**, *100*, 1350–1355. [CrossRef]

26. Guo, Z.; Gao, X.; Wang, W.; Li, G.; Duan, Z.; Shi, H. S-Wave Velocity of the Crust around Tianshan Mountains Inverted from Seismic Ambient Noise Tomography. *Chin. Sci. Bull.* **2010**, *55*, 3590–3598. [CrossRef]
27. Zhang, X.; Song, X.; Li, J. A Comparative Study of Seismic Tomography Models of the Chinese Continental Lithosphere. *Earthq. Sci.* **2022**, *35*, 161–185. [CrossRef]
28. Zhang, Z.; Liu, Y.; Yao, H.; Feng, J.; Tang, M.; Wang, W. 3-D Velocity Model of the Crust and Uppermost Mantle beneath Xinjiang Region, Constructed by Joint Tomography of Body and Surface Wave Data. *Sci. China Earth Sci.* **2026**, *69*, 788–804. [CrossRef]
29. Zhang, Z.; Liang, C.; Cao, F.; Fan, X.; Wei, B. Crustal Deformation and Uplift Mechanisms in the Central-Eastern Tien Shan Constrained by Seismic Ambient Noise Tomography. *Tectonics* **2026**, *45*, e2025TC009162. [CrossRef]
30. Xin, H.; Zhang, H.; Kang, M.; He, R.; Gao, L.; Gao, J. High-Resolution Lithospheric Velocity Structure of Continental China by Double-Difference Seismic Travel-Time Tomography. *Seismol. Res. Lett.* **2018**, *90*, 229–241. [CrossRef]
31. Taborda, R.; Azizzadeh-roodpish, S.; Khoshnevis, N.; Cheng, K. Evaluation of the Southern California Seismic Velocity Models through Simulation of Recorded Events. *Geophys. J. Int.* **2016**, *205*, 1342–1364. [CrossRef]
32. Ma, J.; Bunge, H.P.; Thrastarson, S.; Fichtner, A.; van Herwaarden, D.P.; Tian, Y.; Chang, S.J.; Liu, T. Seismic Full-Waveform Inversion of the Crust-Mantle Structure Beneath China and Adjacent Regions. *J. Geophys. Res. Solid Earth* **2022**, *127*, e2022JB024957. [CrossRef]
33. Gao, H.; Shen, Y. Validation of Recent Shear Wave Velocity Models in the United States with Full-Wave Simulation. *J. Geophys. Res. Solid Earth* **2015**, *120*, 344–358. [CrossRef]
34. Zhou, T.; Xi, Z.; Chen, M.; Li, J. Assessment of Seismic Tomographic Models of the Contiguous United States Using Intermediate-Period 3-D Wavefield Simulation. *Geophys. J. Int.* **2022**, *228*, 1392–1409. [CrossRef]
35. Fang, H.; Zhang, H.; Yao, H.; Allam, A.; Zigone, D.; Ben-Zion, Y.; Thurber, C.; van der Hilst, R.D. A New Algorithm for Three-Dimensional Joint Inversion of Body Wave and Surface Wave Data and Its Application to the Southern California Plate Boundary Region. *J. Geophys. Res. Solid Earth* **2016**, *121*, 3557–3569. [CrossRef]
36. Kennett, B.L.N.; Engdahl, E.R.; Buland, R. Constraints on Seismic Velocities in the Earth from Traveltimes. *Geophys. J. Int.* **1995**, *122*, 108–124. [CrossRef]
37. Bensen, G.D.; Ritzwoller, M.H.; Barmin, M.P.; Levshin, A.L.; Lin, F.; Moschetti, M.P.; Shapiro, N.M.; Yang, Y. Processing Seismic Ambient Noise Data to Obtain Reliable Broad-Band Surface Wave Dispersion Measurements. *Geophys. J. Int.* **2007**, *169*, 1239–1260. [CrossRef]
38. Christensen, N.I.; Mooney, W.D. Seismic Velocity Structure and Composition of the Continental Crust: A Global View. *J. Geophys. Res. Solid Earth* **1995**, *100*, 9761–9788. [CrossRef]
39. Zhu, L.; Rivera, L.A. A Note on the Dynamic and Static Displacements from a Point Source in Multilayered Media. *Geophys. J. Int.* **2002**, *148*, 619–627. [CrossRef]
40. Shearer, P.M. *Introduction to Seismology*, 2nd ed.; Cambridge University Press: Cambridge, UK, 2009.
41. Zhu, L.; Helmberger, D.V. Advancement in Source Estimation Techniques Using Broadband Regional Seismograms. *Bull. Seismol. Soc. Am.* **1996**, *86*, 1634–1641. [CrossRef]
42. Laske, G.; Masters, G.; Ma, Z.; Pasyanos, M. Update on CRUST1. 0-A 1-Degree Global Model of Earth ' s Crust. In *Geophysical Research Abstracts*; Copernicus Publications: Göttingen, Germany, 2013; Volume 15, p. 2658.
43. Xin, H.; Zhang, H.; Gao, L.; Han, S.; Fang, H.; Zhang, G. Three-Dimensional Lithospheric VP/VS Structure Beneath Chinese Continent. *Seismol. Res. Lett.* **2025**, *96*, 1758–1779. [CrossRef]
44. Wessel, P.; Luis, J.F.; Uieda, L.; Scharroo, R.; Wobbe, F.; Smith, W.H.F.; Tian, D. The Generic Mapping Tools Version 6. *Geochem. Geophys. Geosystems* **2019**, *20*, 5556–5564. [CrossRef]

Disclaimer/Publisher's Note: The statements, opinions and data contained in all publications are solely those of the individual author(s) and contributor(s) and not of MDPI and/or the editor(s). MDPI and/or the editor(s) disclaim responsibility for any injury to people or property resulting from any ideas, methods, instructions or products referred to in the content.